ARTICLE

https://doi.org/10.1590/2317-4889202220220029

BJGEO
Brazilian Journal of Geology

Turbidity currents generating lobes: flow rate influence on 3D experiments without slope break

Tulio Machado Humberto Guimarães[1]*, Débora Karine Koller[1], Juan Jose Fedele[2], Rafael Manica[1]

Abstract

Turbidity current hydrodynamic properties are evaluated experimentally to understand the formation of turbidity current depositional lobes and the relationship with flow properties, in particular, flow rates. This study focused on the depositional behavior of unconfined turbidity currents through the analysis of three-dimensional experiments performed in a large-scale channel-basin tank without slope break. Three flow rates were simulated when flow velocities, both in longitudinal and transversal directions, were measured and resulting depositional features were evaluated. The three-dimensional physical experiments carried out in this work allowed the identification of two flow rate models with different hydrodynamic characteristics and two distinct lobes. Lower flow rates produced elongated lobate deposits, with characteristic lower flow regime plane bed on the surfaces, characteristic downstream sediment fining that resulted from lower flow velocities, and visibly less turbulent flows from less competent and waning turbidity currents. Higher flow rates showed a more characteristic radial and downstream fining sediment with lobe surfaces displaying ripples and dunes, generated by the higher flow velocities, presumably more turbulent, and more competent turbidity currents.

KEYWORDS: physical modeling; turbidity currents; lobes; flow rate.

INTRODUCTION

Turbidity currents are subaqueous flows formed by mixtures of sediment and water that render the mix heavier than surrounding (or ambient) water and can potentially run for very long distances, covering continental slopes to abyssal plains. These currents can become highly erosive in their way (Shepard 1981), re-entraining or reworking previously deposited sediments that then can become part of the flow, increasing their driving force. Turbidity currents can flow for minutes to weeks (Azpiroz-Zabala *et al.* 2017) and commonly display velocities ranging from 0.5 to 6 m/s (Cooper *et al.* 2013, Xu *et al.* 2014, Talling *et al.* 2022). Much less is known about the flow properties and velocities when turbidity currents become unconfined. As also shown by recent field measurements, large-scale turbidity currents can travel long distances, for example > 100 km before sedimentation in unconfined settings takes place (Stevenson *et al.* 2018, Talling *et al.* 2022). As a consequence, turbidity currents form preferential paths, building submarine channels or canyons along areas with high slopes. According to Leeuw *et al.* (2016), confined regions can progressively evolve from a depositional or erosional process, promoting a gradual increase in sediment bypass on the slope. After traversing steep slope-confined paths, i.e., channels, turbidity currents typically lose confinement as part of the natural evolution of the turbiditic system, where sedimentation of the transported material takes place, forming turbidity lobes. Generally, between the confined and unconfined zones, there may be a transition region — the channel lobe transition zone (Piper and Savoye 1993, Postma *et al.* 2016), marked by slope break and the occurrence of hydraulic jumps (Komar 1971), in some cases.

The hydrodynamic and associated sediment transport processes that characterize the unconfined portions of turbidity current systems are unclear and largely unknown, remaining, as a consequence, speculative, from interpretations of limited outcrop analysis and data. According to Pohl *et al.* (2019), when the flow expands radially, a lateral pressure gradient is formed, as the turbidity current is denser than the ambient fluid, and this pressure gradient is higher near the bottom. As a result, there is a rapid lateral expansion and a decrease in velocity along the central axis of the current, which in turn alters and changes the evolution of the flow and thus associated sedimentologic processes. The three-dimensional nature of the problem becomes key and cannot be ignored as it most likely determines the fundamental behavior of the flows.

Sedimentary deposits of turbidity currents, commonly referred to as lobes, typically associated with regions where parent flows have flowed unconfined (Normark 1970, Jobe *et al.* 2015), have been of great interest for the oil and gas

Supplementary data

Supplementary data associated with this article can be found at Supplementary Material 1.

[1]Universidade do Rio Grande do Sul – Porto Alegre (RS), Brazil.
E-mails: machado_tulio@hotmail.com, debora.koller@ufrgs.br, manica@iph.ufrgs.br

[2]ExxonMobil – Houston (TX), United States of America.
E-mail: juan.j.fedele@exxonmobil.com

*Corresponding author.

industry due to their potential for high-quality hydrocarbon reservoirs. Mulder and Etienne (2010) defined lobes as the most distal (final) deposits of siliclastic turbidity systems, which can be found not only further beyond the continental rise (basin-floor lobes) but also perched on mid-to-low continental slopes (intra-slope lobes). These configurations were also observed in the Karoo Basin — South Africa (Hodgson 2009) and in the Golo System — France (Sweet *et al.* 2019). In this sense, identifying, characterizing, and understanding the mechanisms of the formation of these deposits become significant (Pettingill 2004).

Less is known in regard to the effects of loss of flow confinement, e.g., velocity, flow thickness, and concentration changes, as currents spread laterally and keep moving forward for some distance before they die out. Spychala *et al.* (2020) found that discharge is the key factor controlling the onset of lobe element deposition while the basin-floor angle and sediment volume concentration have a great influence on the geometric characteristics of the lobes (Luthi 1981, Piper and Normark 2009, Talling *et al.* 2013, Clare *et al.* 2016). To better understand these processes linking the flow and resulting depositional features, we developed a study where the flow rate was varied, the detailed velocity measurements of the flows, over a large area, were included, and our results are presented herein.

Physical simulation and laboratory experiments have been a key tool aiding progress in the understanding of density and, in particular, turbidity current hydraulics and associated sediment transport processes (Middleton 1966, Kneller and Buckee 2000, Manica 2012). 3D-controlled experiments using turbidity currents allow us to generate depositional features (lobes) and link these deposits to the hydrodynamic properties of flows, including flow rate (Luthi 1981, Manica *et al.* 2006). Keeping in mind the important limitations of the laboratory results due to scaling and the use of dimensionless ratios (Reynolds, Shields, Rouse, densimetric Froude numbers) to guide experimental design, we assume that some of the fundamental features observed in our experiments do have an analogous counterpart and thus can be extrapolated to the natural environment.

This work aimed to evaluate experimentally the effects of turbidity current hydrodynamic properties on the formation of lobes through the variation of the injected flow rate. Also, it aimed to reproduce the region immediately beyond the unconfined turbidity currents to document the effects of the flow spread on lobe formation. 3D experiments were performed in a large-scale basin tank consisting of an incoming channel carrying the turbidity current, ending in a large plate, without slope break, where flows freely flowed unconfined. We highly concentrated on the measurements of flows and established relationships between longitudinal and transversal flow velocities and lobe dimensions, which are all reported in this study.

APPARATUS AND METHODOLOGY

The 3D tank used for the experiments is a masonry and concrete channel-basin unit with a 46 m^3 capacity for water (Fig. 1). A confined region (channel) has a chute that represents the natural configuration of a submarine channel, ending in an open, wide plate mimicking the basin. Inside this large tank, the basin floor has three adjustable smaller plates that can be set to different slopes, one plate including the confined region (1.5 m long × 0.20 m wide) and the other two for the basin (3 m long × 3 wide). For this set of experiments, the initial slope of all plates was constant and fixed at 4º (i.e., no-slope break), and the water level was fixed to submerge the entire setting. An elevated auxiliary reservoir (5 m^3) with an electromechanical stirrer was used for the preparation of the water-sediment mixtures that formed the turbidity flows. A system of pipes and an electromagnetic flowmeter device allowed for the control of the discharge of the mixtures injected into the tank.

The water-sediment mixtures used to generate the experimental turbidity currents were composed of water (ρ = 998 kg m^{-3}) and mineral coal (ρ_s = 1,450 kg m^{-3}). This mineral coal presented poorly sorted grains with d_{10}, d_{50}, and d_{90} of 9.54, 36.69, and 75.64 μm, respectively. The simulated turbidity currents were initially set in the mixing tank with approximately 5% volumetric concentration (C_{vol}) and were thus classified as Newtonian (Castro *et al.* 2021) low-density turbidity currents (Mulder and Alexander 2001, Manica 2012).

Four acoustic Doppler velocimetry (ADV) probes were used in the experiments. They measured the velocity at one point in three directions (X, Y, and Z). One ADV was installed 50 cm from the injection point (confined channel) and the other three in the basin, positioned laterally on the left and right (100 cm from the central axis) and at the center axis of the tank. The ADVs were fixed in a movable structure that allowed their movement along longitudinal (X) and vertical (Z) directions at 50 cm (or 200 cm from injection), 150, 250, and 350 cm from the unconfined region (Fig. 1). In each position, the first point of velocity measurement of the three aligned ADVs (100 cm right, central, and 100 cm left) was always 1 cm from the bed. After 1 min of data measurement, the three ADVs were simultaneously moved up 1 cm and another set of 1-min data was recorded. This procedure was repeated until the height of 8 cm from the bed. In the end, the measurements covered eight distinct points distributed throughout the basin, except one in the channelized zone. In addition, pictures were taken from the top using a camera positioned 4 m above the center line of the tank, every 5 s.

The three experiments followed the same methodology. The 3D tank was filled with up to 1 m of water (ambient fluid). The 5% C_{vol} mixture was prepared in the auxiliary reservoir and injected continuously into the tank with three different flow rates: E10 = 10 L/min, E30 = 30 L/min, and E40 = 40 L/min. The ADVs registered the evolution of flow velocities in the basin domain by the procedure described above, while the camera registered the current front advancement and flow evolution in time.

After 1 h (for all runs), the injection was stopped and the tank was left still to allow the turbidity currents to completely die off and the lingering suspension to completely settle. After 48 h, the tank was slowly drained to avoid any remobilization and to limit deposit deformation as much as possible. The total time of draining was typically 10 days. The deposit

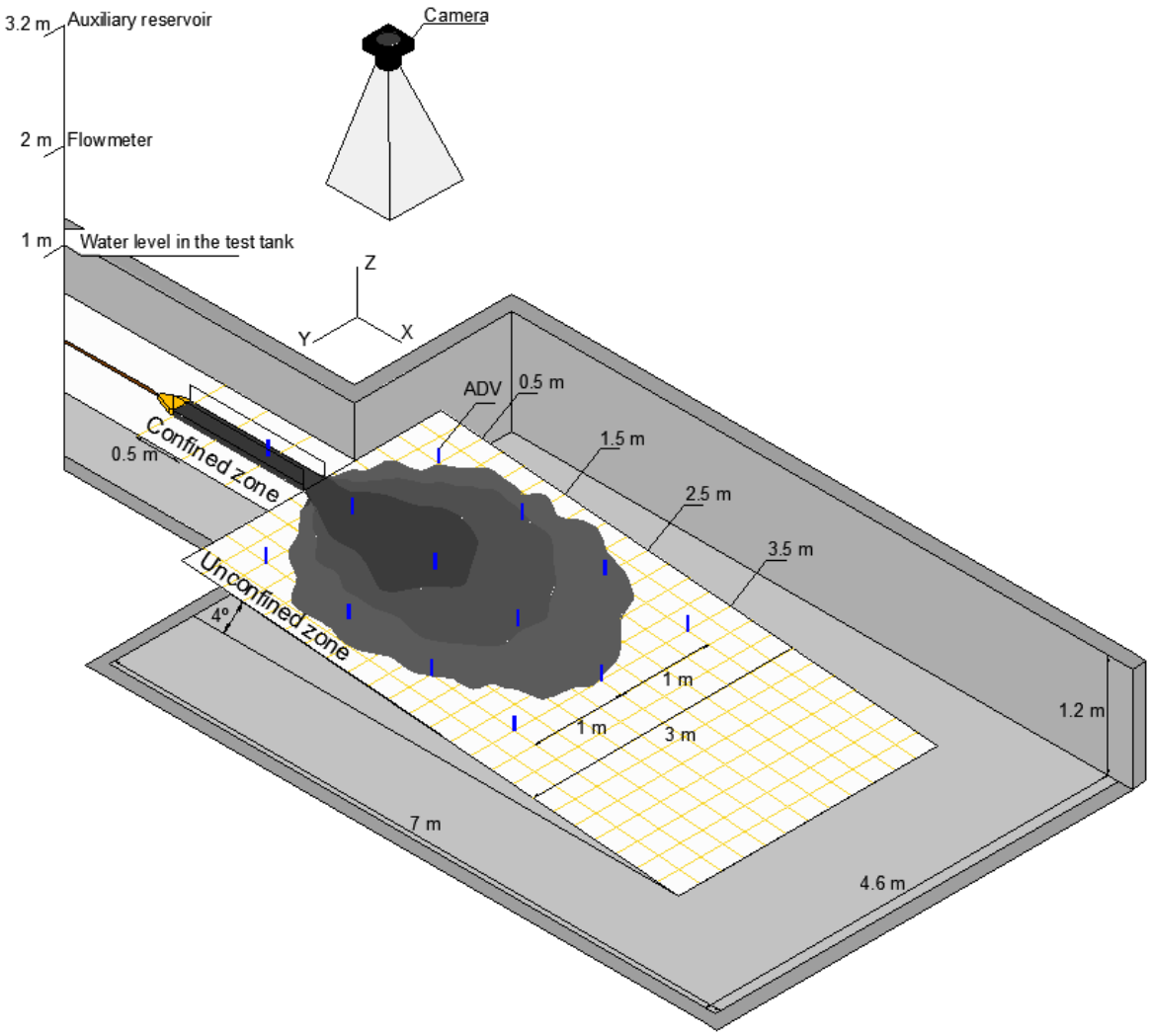

Figure 1. 3D channel-basin tank and the experimental facility (the blue sticks represent the ADV positions).

was photographed and more than 80 sediment samples from the deposits were collected every 20 cm along the longitudinal (X) and transversal (Y) directions (forming a grid) in each case. Finally, the samples were processed on a CILAS 1,180 grain-sized laser particle device (with a range for accurate readings between 0.04 and 2,500 mm).

RESULTS

Confined Channel zone

One of the hydrodynamic parameters of the turbidity current that is addressed in this study is the mean vertical velocity profile registered by the ADVs. Figure 2 displays both longitudinal (X) and transversal (Y) mean profiles measured in the confined channel zone.

The longitudinal (X) vertical velocity profile in run E10 presented a classical behavior of low-density turbidity currents (Altinakar *et al.* 1996, Kneller and Buckee 2000, Manica 2012). The maximum value is close to the bed (at a height of 0.1 cm), and the velocities rapidly decrease toward the upper part of the flow. Above the velocity max locus, the registered velocities were typically only about 10% of the maximum. On runs E30 and E40, the flows were thicker than those

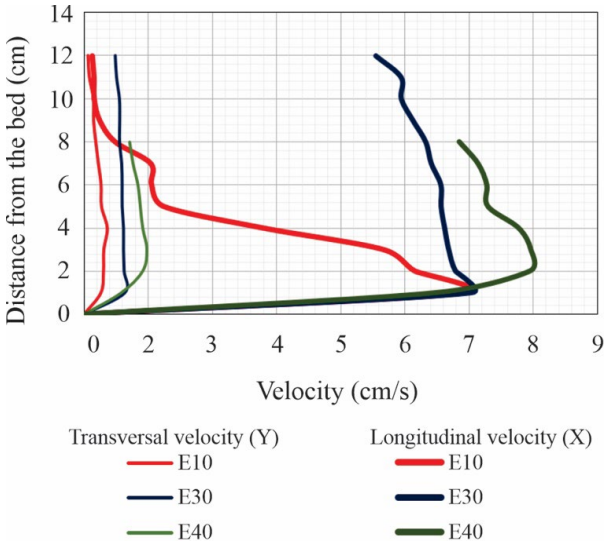

Figure 2. Mean vertical velocity profiles of the channel zone for the three runs: longitudinal (X) velocities (thick lines) and transversal (Y) velocities (thin lines).

observed in E10, and the profiles showed more uniform values along the vertical (i.e., vertical homogeneity), as shown by the low standard deviation values for the velocity (Table 1). Our observations suggest a greater turbulent cloud (mixture) immediately after the injection in all cases, likely related to

jet effects at the injection point (Ferreira 2013); thus, some effects of the transition between an inertia-driven flow at the very input (jet) and gravity-driven (pure turbidity current) might be captured in the confined section, more notable for larger flow rates. At the top of the profile, we noticed a slight reduction in the velocity values. For the transversal velocity (Y), we registered lower values when compared to the longitudinal velocity (X) (from around 1/7 to 1/9). Also, the shape of the profiles shows some vertical uniformity, regardless of the flow rate injected. For both longitudinal (X) and transversal (Y) vertical velocity profiles (Fig. 3), the flow rate presented a direct relationship with the mean (U_{mean}) and maximum (U_{max}) velocities. Apart from the similar values of maximum velocity between E10 and E30 (longitudinal X), as the flow rate increased, the maximum velocity increased as well.

The mean velocity (U_{mean}) was obtained by the (graphical) integration of the vertical profile area (Table 1) and better demonstrates, in our view, the controlling effects of the flow rate on the turbidity currents mechanics within the confined region. By using experiment E10 as a reference (Fig. 3B), we clearly see a direct relation between mean velocity values (U_{mean}) and the increment of the experimental flow rate.

As the flow rate increased (up to four times compared to E10), the increase in the mean velocity value became close to 2.5, i.e., the correlation of these parameters showed nonlinear behavior in relation to the identity line (x = y dashed line). Also, these results indicate a likely upper limit of mean velocities (Fig 3B), when we consider higher values of injected flow rate. On the contrary, the transversal velocity (Y) within the confined zone indicates the opposite, in which the mean values increase faster as the flow rate increases.

Table 1. Mean (U_{mean}) and maximum (U_{max}) velocity from turbidity currents at the channel zone.

Run	Longitudinal (X)			Transversal (Y)		
	U_{max} cm/s	U_{mean} cm/s	Mean std. dev.	U_{max} cm/s	U_{mean} cm/s	Mean std. dev.
E10	12.0	5.50	4.40	0.7	0.73	0.11
E30	12.1	11.96	0.51	1.3	1.27	0.01
E40	14.0	13.89	1.02	2.0	1.97	0.26

Unconfined Basin zone

Flow time evolution was analyzed from the images taken with the camera installed above the tank. Figure 4 shows the progress of the turbidity current front as it flows throughout the basin. In Fig. 4, colored lines represent frontal position at intervals of about 10 s. After about 100 s, turbidity currents reached the lateral edges of the plates, and thus analysis was stopped.

A marked flow rate influence on the shape of the current is clearly observed. For the same time interval (same color of the contour line), run E40 shows a larger spread when compared to E10 (lower flow rate), in all directions. After more than 100 s, the flow covered the basin floor. Longitudinal length (L) and transverse advance (W) of the turbidity current were measured at different time intervals to verify the overall geometric planform of the advance (here named as flow shape factor [FSF] = L/W). The measurements of the length and width of the current are plotted in Fig. 5).

For all runs, a direct linear relationship between the length (L) and width (W) of the flow advance was observed. The higher values of the determination coefficient (R^2) confirmed the good-fitted linear trend. By correlating all the angular coefficients of the equations (Fig. 5) with the flow rate (Q), an equation for the flow width as a function of the flow rate (Eq. 1) is proposed using these experimental data:

$$W = [0.2867.\ln(Q) - 0.057].L \quad (1)$$

Where:
W: the width of the turbidity current spread (cm);
Q: the mixture flow rate injected (L/min);
L: the length of the turbidity current spread (cm).

As mentioned above, the geometric shape factor (FSF) for all three flows was calculated to further describe the unconfined flow; the obtained values suggest that the higher the FSF becomes, the more elongated the flow tends to be, whereas

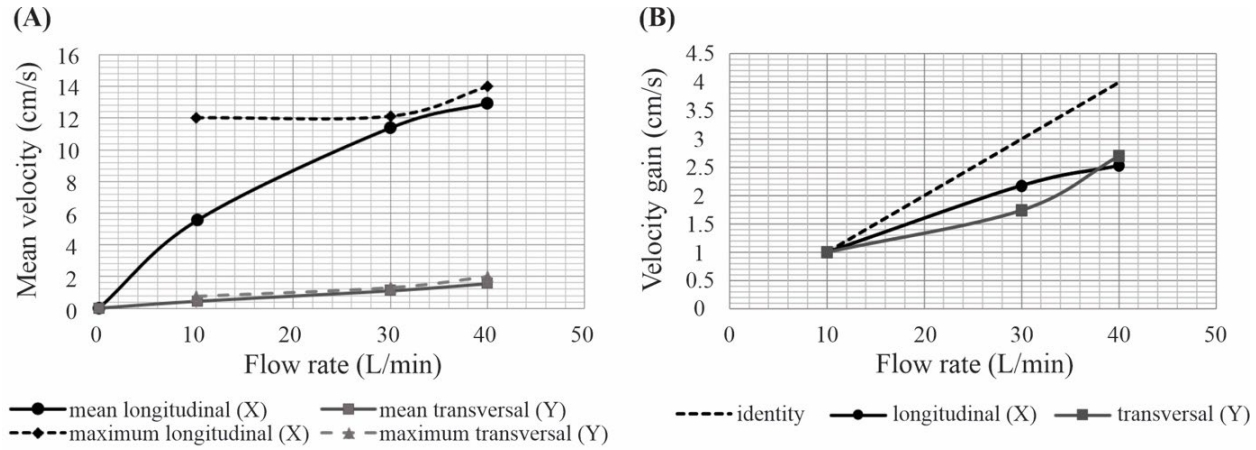

Figure 3. (A) Mean and maximum velocity of the turbidity current at the channel zone related with the flow rate and (B) velocity and flow rate gain related to E10 run.

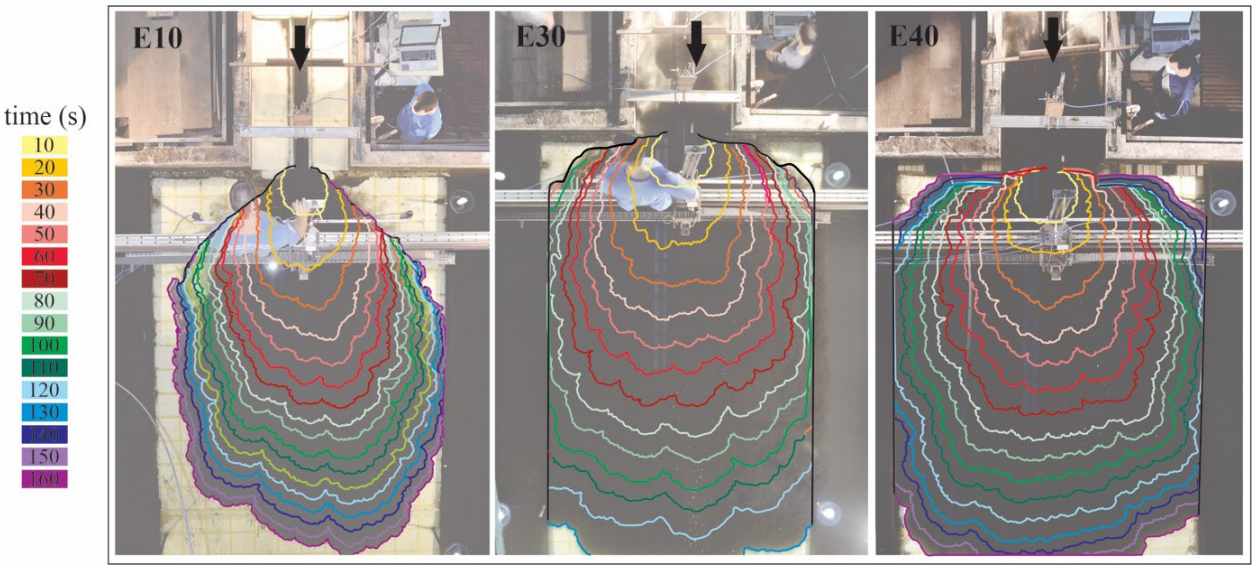

Figure 4. Turbidity current evolution in the basin is registered by lines drawn every 10 s for the three-run simulation.

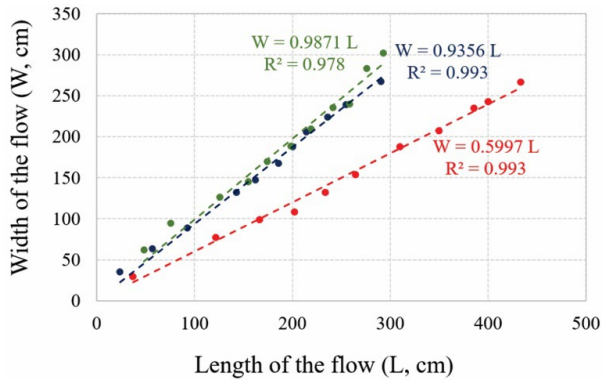

Figure 5. Relationship between the length (C) and width (L) of the flow.

for cases of FSF close to 1, it indicates a more radial flow tendency. Figure 6A presents a plot of the FSF as a function of time, and Fig. 6B presents the mean FSF versus flow rate (Q). These plots suggest that, regardless of the flow rate, the FSF increased up to a time of 40 s after flow reached unconfinement and then tended to keep constant values (up to 100 s). For run E10 (low-flow rate), the FSF is higher than that observed in E30 and E40, which implies an elongated form of turbidity current for this particular low-flow run (e.g., prevailing downflow velocities). In contrast, runs E30 and E40 (higher flow rates) showed more radial shapes (FSF close 1), thus suggesting comparable values for down-axis and lateral velocity values.

Longitudinal velocities (X)

Figure 7 shows the vertical distribution of the longitudinal velocity (X) of the turbidity current at four locations over the basin (50, 150, 250, and 350 cm). Also, the velocity vertical distribution was plotted for the ADVs positioned at 100 cm on the right of the central axis of the basin, on the central axis itself, and at 100 cm on the left of the central axis of the basin (for location references, see Fig. 1).

Along the central axis of the basin, the values of maximum velocities decreased, and thus the gravitational effect of the slope was not sufficient to maintain or accelerate the turbidity currents down to the basin. We noticed an increment in maximum velocity as the flow rate increased, and also an increase in the height of the maximum velocity as the turbidity currents flowed away from the initial confinement-loss point (end of channel). This result is likely due to the initial overall thickening of the flow and bed roughness effect, as indicated by Simpson (1972) and Fabian (2002).

The longitudinal velocities (X) on the lateral lines of the basin (positioned at 100 cm to the right and left of the center) show lower velocities compared to the center line. The first vertical profiles (50 cm into the basin) developed low maximum velocities as the flow started to spread (Fig. 4). Then, velocities increased, evolving to a characteristic unconfined flow. At the last two evaluated positions (250 and 350 cm into the basin), similar maximum velocities were observed, indicating little gain in velocity as the turbidity current flowed downward. Similarly to the results along the center line, the height of maximum velocity increased with distance. Regardless of the position in the basin, the various flows tested indicate a direct relationship between flow rate and velocity. As the flow rate increased, the velocity also increased, as commonly expected.

Depth-averaged (mean) longitudinal velocities (X) were calculated from measured profiles as indicated above. Regardless of the input flow rate, all turbidity currents showed a strong deceleration throughout the central axis of the deposit due to sedimentation of particles and the formation of the lobe. The increase in the longitudinal velocity (X) on the lateral lines of the basin (100 cm right and left from the center line) was also observed in the longitudinal direction (X).

From the results presented in Figs. 7 and 8 (see also Suppl. Mat. A), we calculated the main flow nondimensional parameters using input concentration and measured flow conditions at the point where currents become unconfined (end of the channel), namely, Reynolds number (Re) and the densimetric

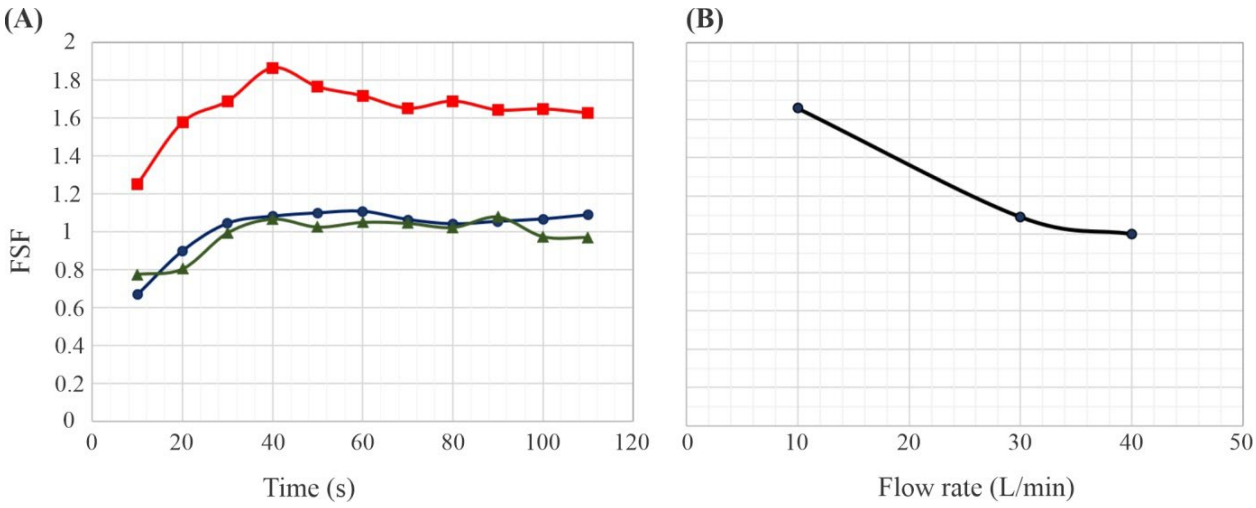

Figure 6. (A) Flow shape factor (FSF) along the time for all runs. (B) Mean FSF related to the injection flow rate.

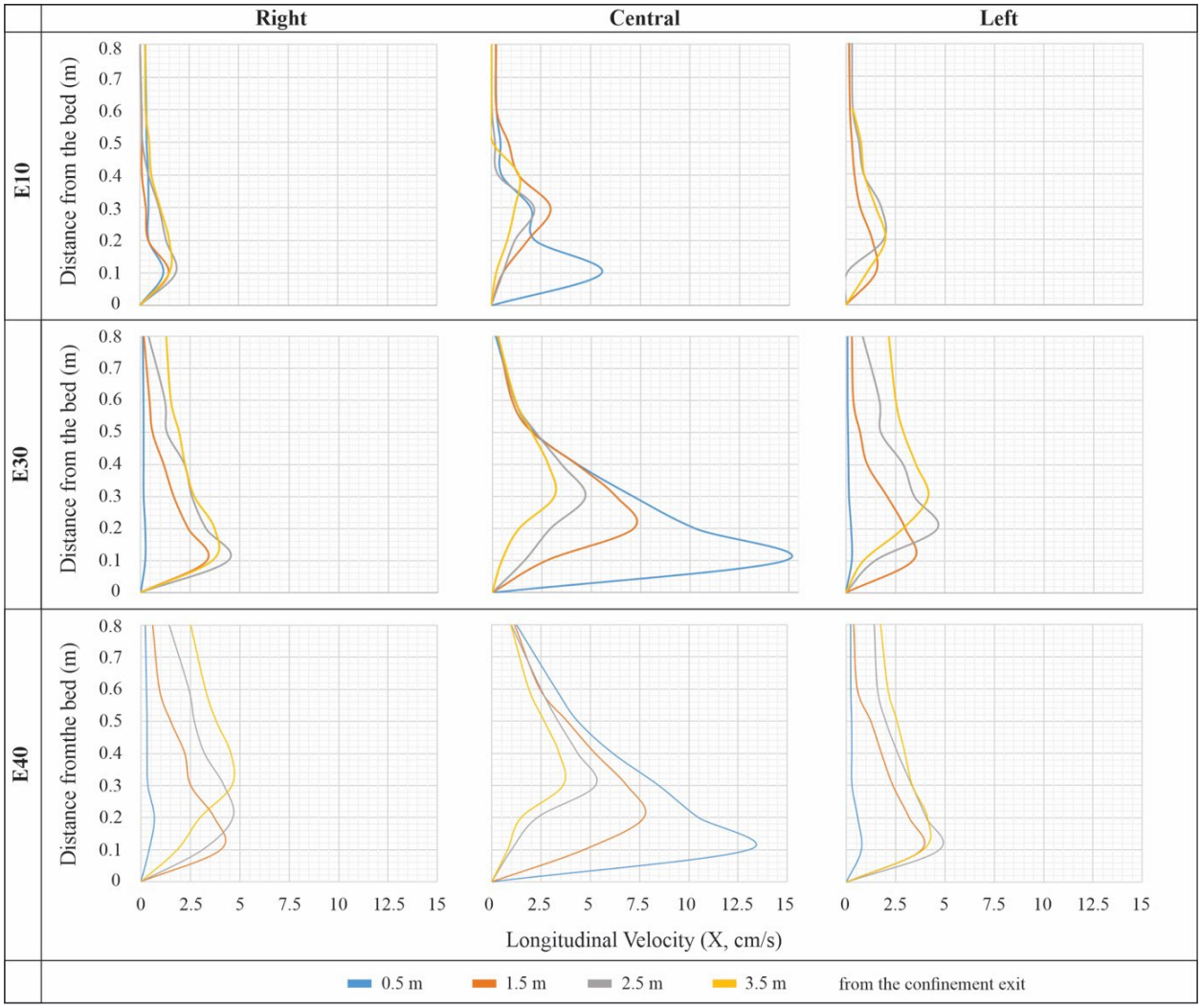

Figure 7. Mean and maximum vertical longitudinal velocity profiles of the turbidity current at the basin zone for all runs and all ADVs positioned in the basin (see Fig. 1).

Froude number (F_{rd}) (Middleton 1966). Table 2 presents these parameters at the center line of the flow, immediately after unconfinement starts, as mentioned already. Specifically, the thickness of the turbidity current (H) was estimated visually from the vertical profiles, whereas turbidity current bulk volumetric concentrations (C_{vol}) were estimated assuming a roughly 20% reduction of the mixture suspended sediment concentration C_{vol} due to dilution and sedimentation of the particles along the confined channelized zone (concentration of suspended sediment was not sampled). The kinematic

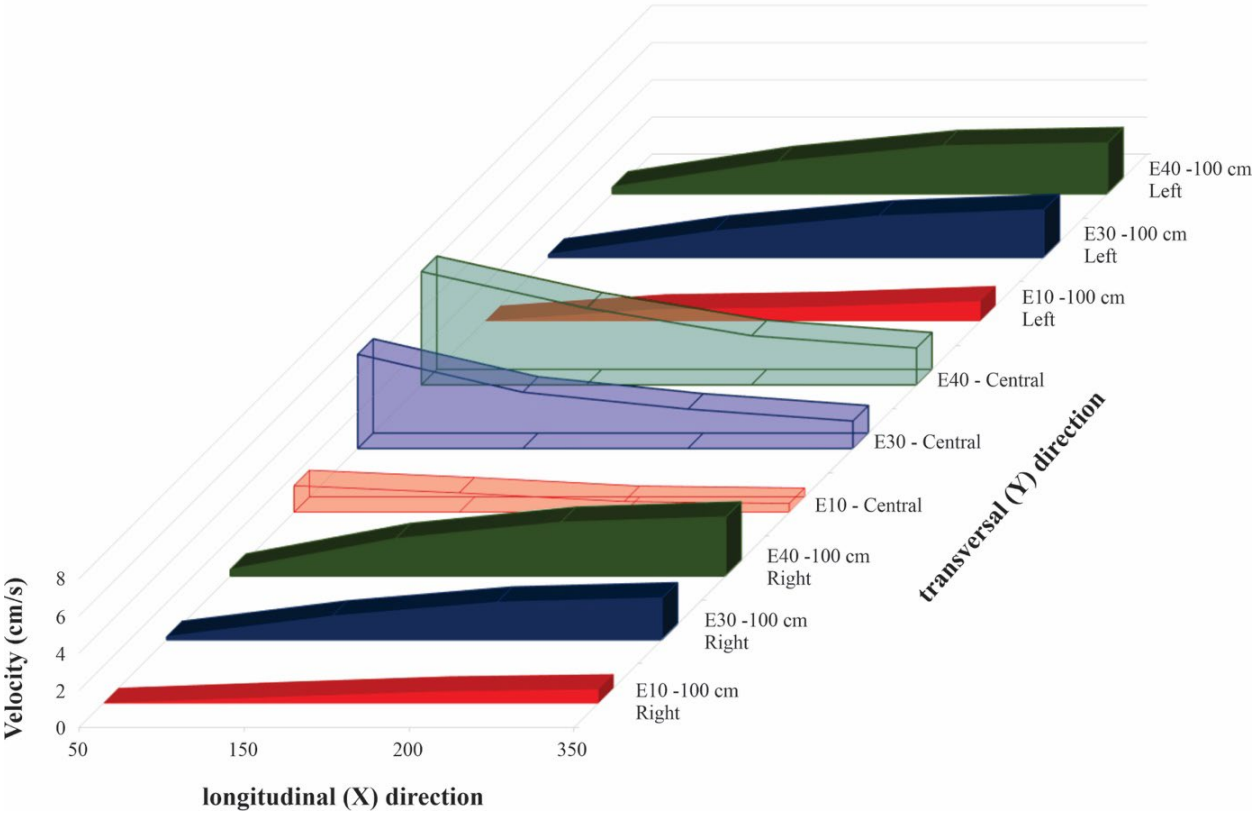

Figure 8. Mean and maximum longitudinal (X) velocity of the turbidity current along the distance in the basin in the three ADVs positions (100 cm right, at central axis, and 100 cm left).

Table 2. Nondimensional parameters Reynolds number (Re) and densimetric Froude number (Fr_d).

Run	U_{max}	H	$\nu \times 10^{-6}$	$C_{vol\ adopted}$	$\Delta\rho/\rho$	Re	Fr_d
	(m/s)	(m)	(m^2/s)	(%)	(-)	$U_{max} \times H/\nu$	$U_{max}/(\Delta\rho/\rho \times 9.8 \times H)^{0.5}$
E10	0.055	0.05	1.37	4	0.0181	520 Laminar < 500	0.59 Subcritical < 1
E30	0.148	0.07	1.37	4	0.0181	2,584 Turbulent > 2,000	1.33 Supercritical > 1
E40	0.130	0.07	1.37	4	0.0181	3,106 Turbulent > 2,000	1.17 Supercritical > 1

viscosity (ν) was calculated using the equation proposed by Castro *et al.* (2021).

The first-order approximation of the nondimensional parameters indicates low turbulence (transition or even laminar) and subcritical flow for run E10 at the analyzed location, while for the higher flow rates (E30 and E40), the flow regimes were supercritical and turbulent. We speculate that due to smaller discharge and velocities, run E10 might be the most difficult to scale up to real conditions, particularly when considering channel-lobe transition settings, even for low gradient turbiditic deposits.

Transversal velocities (Y)

Figure 9 shows the transversal (Y) velocity vertical profile for all runs, representing the spreading velocity of advance in the normal direction (transversal) of the flow (Y axis).

The transversal (Y) velocity profiles show a distinct behavior compared to the longitudinal (X) profiles. Apart from the initial stages of unconfinement (50 cm blue line), where the flow started to spread, the profiles present lower and more constant velocities along the vertical. This effect is clearly observed as the distance from the unconfined increases. The maximum velocity was reduced from 3 to 0.5 cm/s along the central axis, for example; the peak of maximum velocity was preserved in the range of 0.1 to 0.2 cm/s for all profiles. However, in the lateral lines measured, i.e., 100 cm left and 100 cm right from the center, the velocity profiles varied significantly along the distance. The profiles show the classical vertical profile of turbidity currents with a maximum velocity close to the bed, followed by a reduction of values along the vertical above this point. The maximum velocity did not decrease with distance (as on the center line). In fact, the flow expanded laterally and

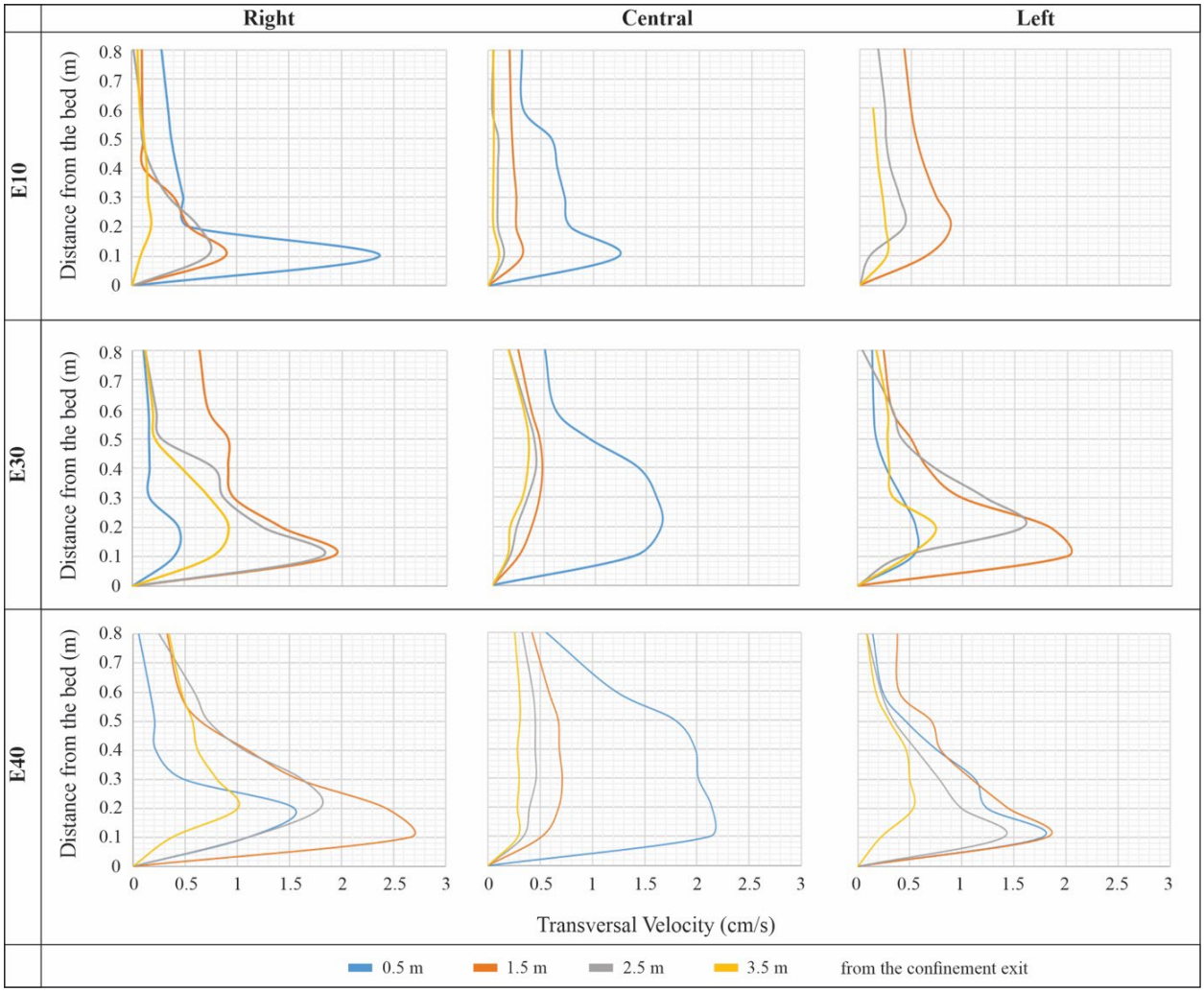

Figure 9. Mean and maximum vertical transversal velocity profiles of the turbidity current at the basin zone for all runs and all ADVs positioned in the basin (see Fig. 1).

accelerated in the first meter of the basin (maximum at 150 cm). It is possible, we argue, that the locally generated slopes due to the deposit presence (maximum length = 150 cm) might have helped accelerate the flow. Then, the flow velocity started to reduce significantly as the distance increased (Fig. 10 and Suppl. Mat. A). In the lateral direction of the flow (i.e., normal to the injection), dilution and deposition of the suspended load of the current might be a simple and physically sound explanation for this behavior. For all profiles, the common observation is, once again, that velocity increased with increased flow rates, as already noted.

Deposits

The lobate deposit's overall final shapes generated by the turbidity currents are given in Fig. 11. The presence (or absence) of bedforms covering the final deposits was noted and used as a means to corroborate flow hydraulic conditions and sedimentary properties of the lobe surfaces (Fig. 11 — lateral view). The deposit created by E10 was devoid of bedforms (presumably due to lower plane bed sediment transport conditions) as a result of low near-bed shear stresses inferred from low velocities measured. The relationship between such flow conditions as very low turbulence and presumably subcritical flows and depositional characteristic imprints for this general setting cannot be generalized from these results (only one isolated run), and thus remains largely unknown. It is currently not considered specifically understood and requires further detailed investigation.

In contrast, ripples and dunes were observed along the deposit generated by E30 and E40 as the flow strength increased visibly for transporting sediments even as bedload, as the flow discharge increased. This most likely resulted in higher near-bed shear stresses and more competent flows capable of transporting coarser particles (silt and fine sand) in the downstream direction (Fig. 12 and Suppl. Mat. A) and thus capable of developing bedforms. Ripples and dunes were observed and reported in the literature under supercritical regime flow conditions in laboratory experiments (Fedele *et al.* 2016, Koller *et al.* 2019).

Based on the images (Fig. 11 — top view), we identified the dimensions of the lobes generated by the turbidity currents and calculated the deposit geometric shape factor (DSF) of the lobe (DSF = L_D/W_D) using the length of the lobe L_D (measured on the central axis) and maximum lobe width (W_D). Figure 13 shows computed DSF values plotted as a function of flow rate and the comparison with the FSF (Fig. 6B).

Experiments E10 and E30 showed an inverse relationship between the DSF and the flow rate. However, the E40 experiment presented a higher value, indicating a direct relationship

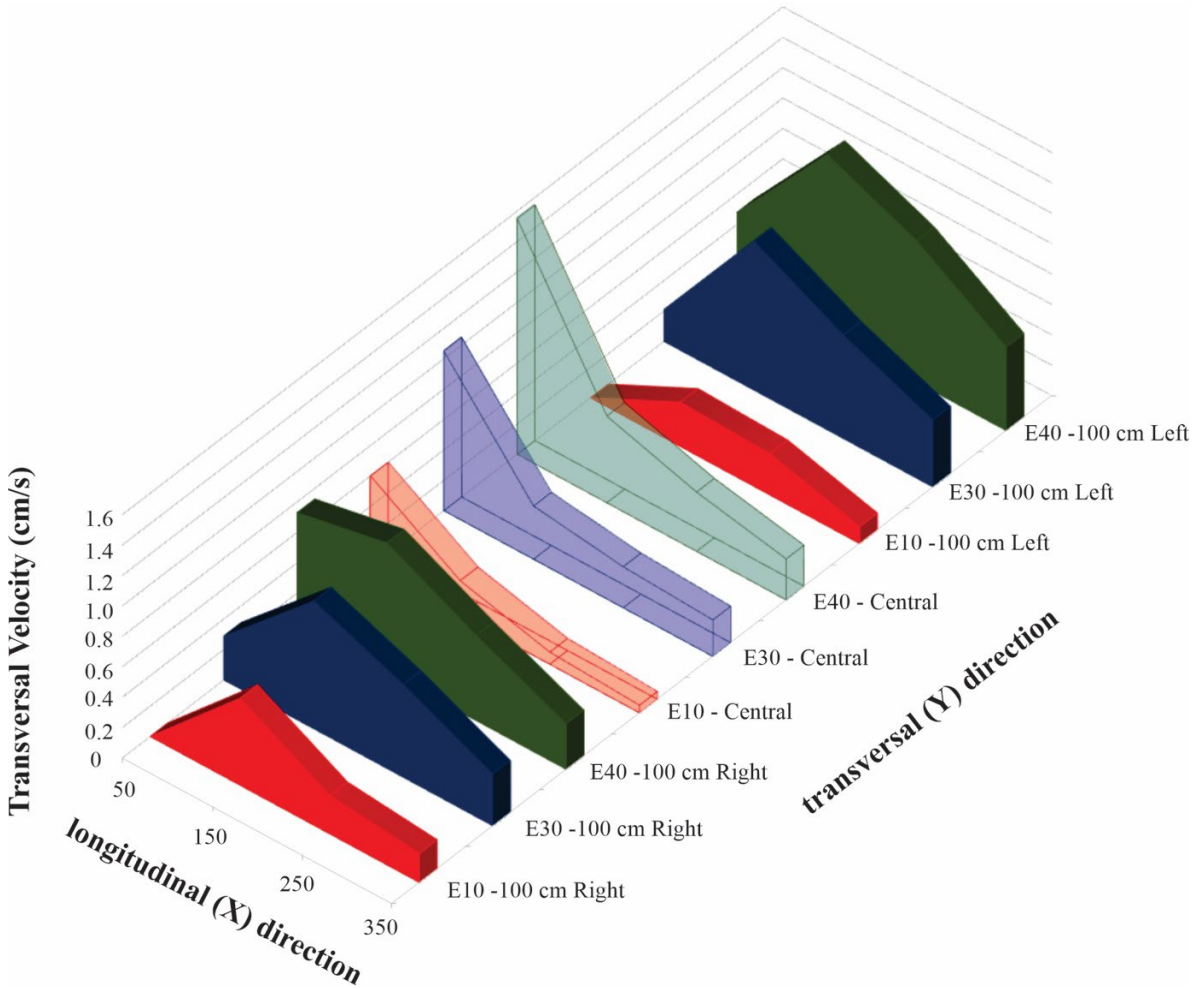

Figure 10. Mean and maximum transversal (X) velocity of the turbidity current along the distance in the basin in the three ADVs positions (100 cm right, at central axis and 100 cm left).

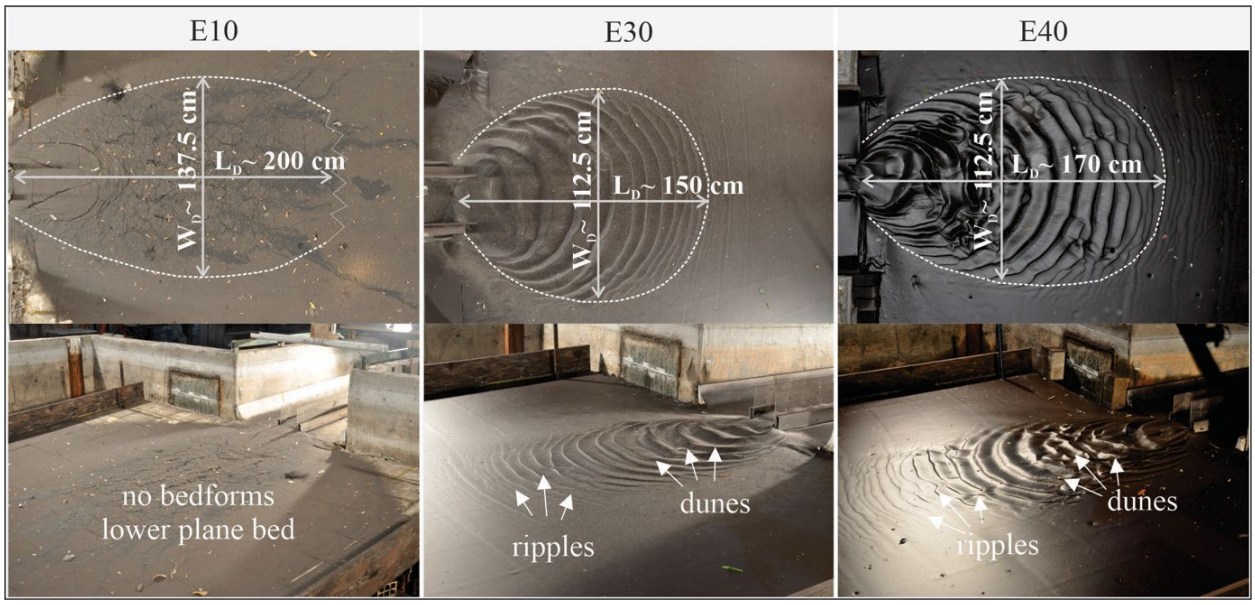

Figure 11. Top-view (above) and lateral view (below) of lobe deposits generated by all three turbidity currents runs (E10, E30, and E40).

with the geometry of the deposit formed. For low-flow rates, the lobe edge in the center line was a bit more ambiguous to determine (Fig. 11 — top left), but nonetheless, we consider the analysis validated. Comparing FSF and DSF values, we noticed that the increase in flow rate (e.g., E30 and E40) results in a more radial current (FSF ~1), while the deposits result in a geometrically more elongated (DSF > 1).

Analysis of sediment size trends was also carried out to complement the study, particularly important for the lobate feature sedimentologic property description. The mean diameter

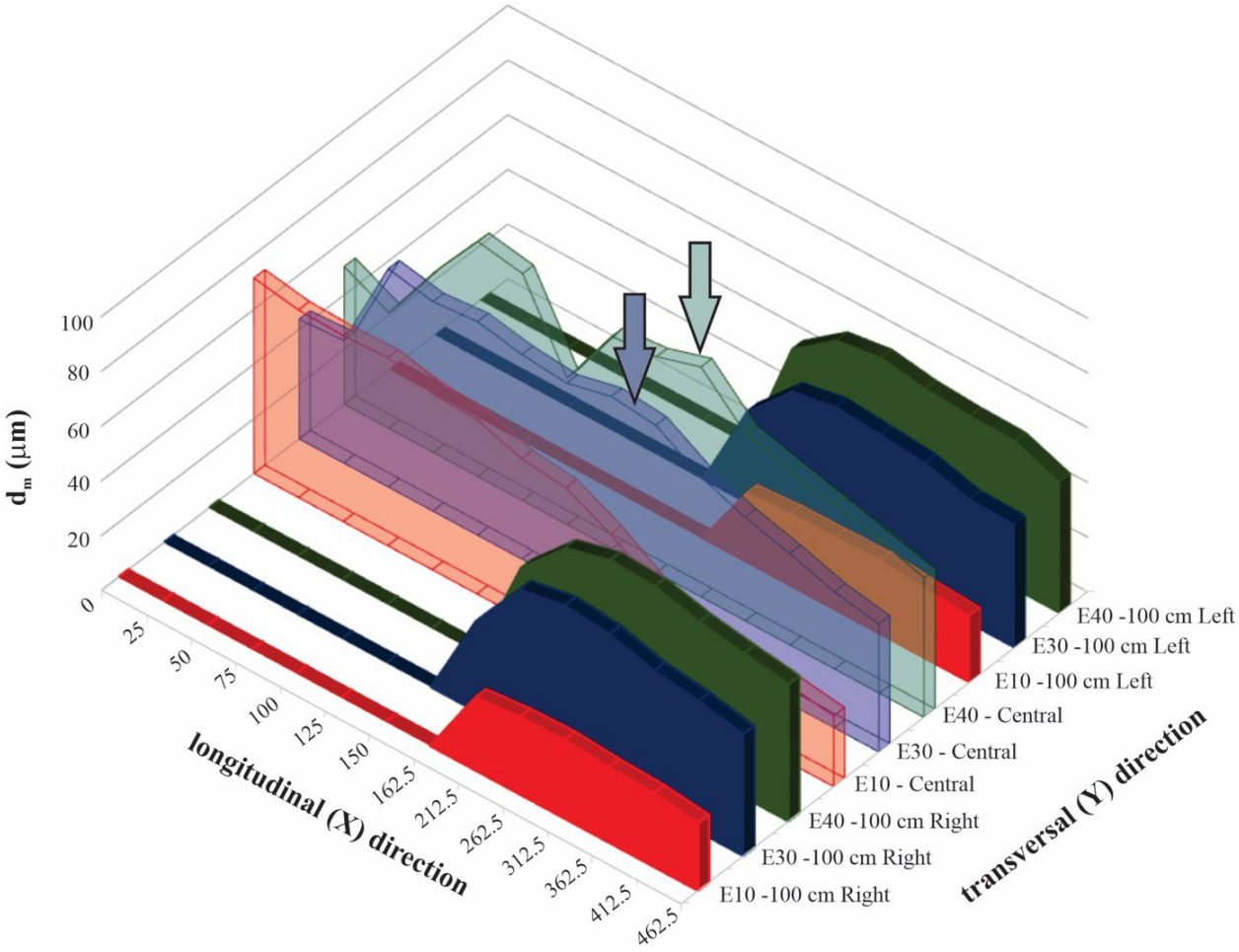

Figure 12. Mean diameter (d_m) of the deposit along the distance (dip section): 100 cm right from the central axis (at the basin), at the central axis (channel and basin): 100 cm left of the central axis (at the basin).

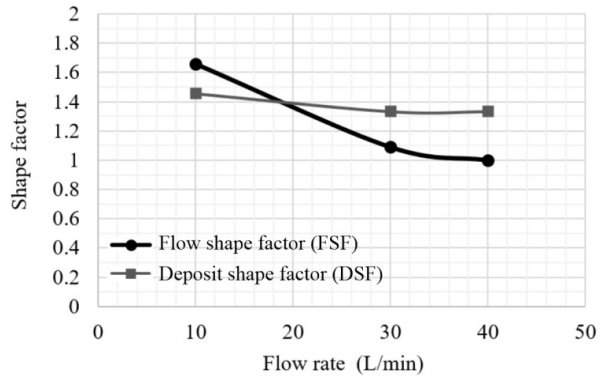

Figure 13. Mean flow shape factor (FSF) and deposit shape factor (DSF) related to the injected flow rate.

(d_m) — calculated by $d_m = (d_{25} + d_{50} + d_{75})/3$ – of the deposit samples collected after draining the tank was plotted against the distance (Fig. 12) from the input point (in-channel) to 312 cm into the basin (or 462 cm total distance of the tank). The lateral lines (100 cm right and 100 cm left from center) were displayed only at the basin zone (Fig. 12).

Considering the samples collected at the central line of the tank, the mean grain size (d_m) showed two distinct behaviors when compared to the flow rate. For the lower flow rate (E10), a clear downstream fining in the deposit was observed from the sample analysis. For this case, we conclude that the turbidity current presented a depositional behavior and waning flow (Kneller 1995) along the downstream distance, and the deposit grain size trend appeared not much affected by the loss of confinement from channel to the basin. Beyond 300 cm from the flow input point, only the finer particles were present in the flow (silt class), as evidenced from the deposit sedimentary composition. On the contrary, for the higher flow rates tested (E30 and E40), the turbidity currents appeared more competent for transporting coarser grains further downstream. A clear effect from the initial jet flow at the input was also observed in the first centimeters (25 cm or so of clear sediment bed and typical bar formation). Just downstream of the initiation of flow unconfinement (from 162 to 212 cm), an increase in mean grain size was noticed (denoted by arrows in Fig. 12). This deposit coarsening was associated with the particularities of channel-lobe transition conditions and subsequent lobe formation and evolution during the experiment, which caused some local trapping of coarser fractions and transportation of finer fractions in suspension beyond this location (proximal lobe). In addition, the length of the lobe in Fig. 11 (L_D ~150 cm) and Fig. 14 matches with the length where this increase in grain size occurred. We speculate that, for E40, a single point did not follow a particular trend (at 125 cm), possibly caused by an experimental error during sampling.

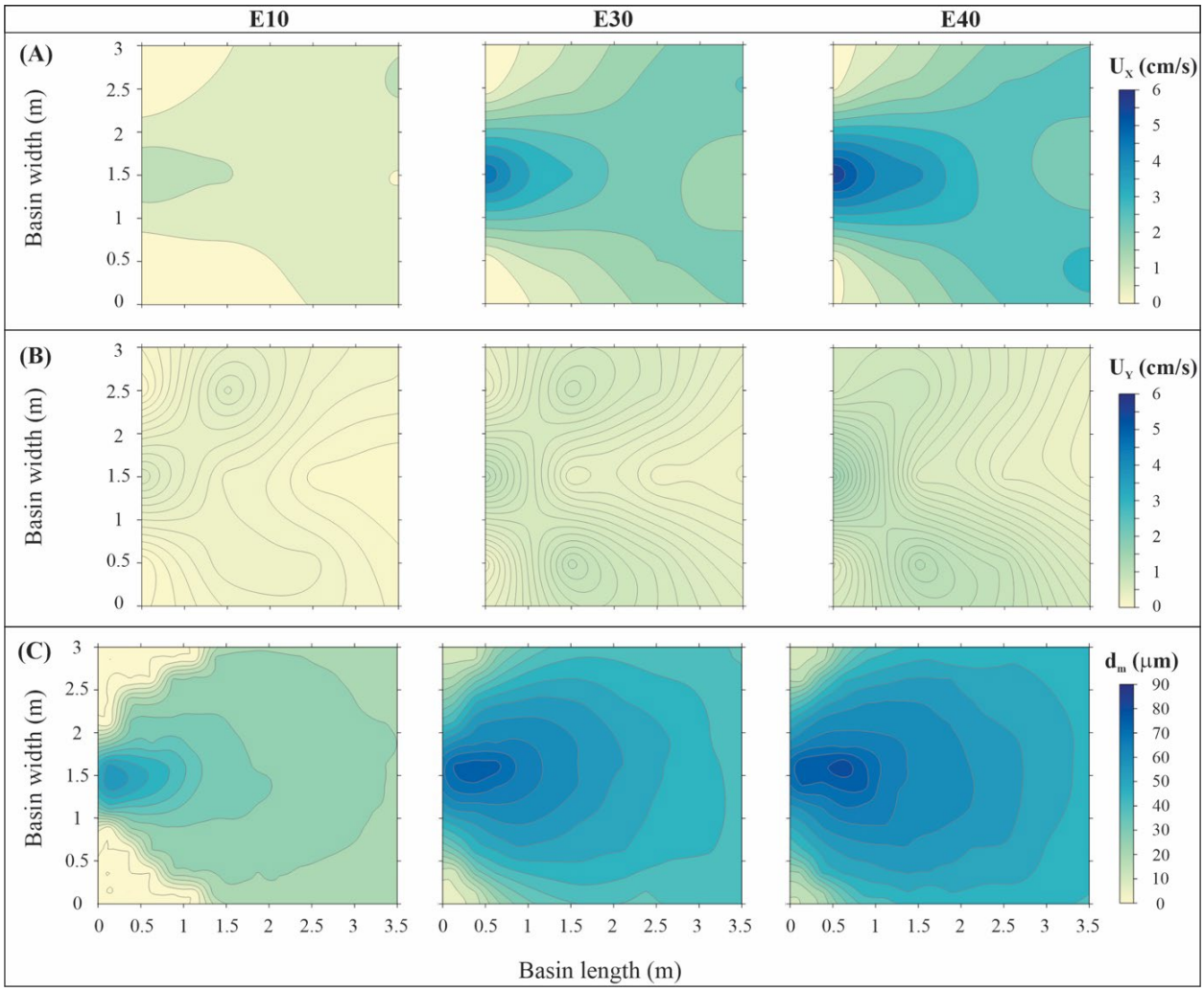

Figure 14. Interpolated contour maps of experimental results: (A) longitudinal velocity (X); (B) transverse velocity (Y); and (C) mean diameter (d_m). Turbidity currents flowed from left to right.

Along the dip lateral lines (100 cm right and 100 cm left from the center), small variations in the mean diameter deposited were observed (Fig. 12) in the downstream direction, presenting in turn lower values compared to those observed along the center line. As these lateral lines are symmetrical in relation to the axis of the tank, we expected and found similarities between the mean diameter (d_m) values. After achieving this distance (100 cm), the flow had settled the suspended load and was not competent to keep the grains in suspension (decreased velocity and turbulence). This behavior was also verified along the center line, as the evaluation in the final distance (462 cm from injection) was found to be similar to the mean diameter (d_m) for each of the flow rates experimented. Finally, we noted the direct influence of flow rate on the mean diameter (d_m), particularly for the low-flow rate test. For E10, d_m was around 50 μm (silt class), and for higher flow rates (E30 and E40), d_m values were close to 80 μm (very fine sand), for the abovementioned location.

Finally, the analysis of the mean diameter along the strike section (transverse) to the flow was performed in proximal (75 cm), central (175 cm), and distal (225 cm) positions relative to unconfinement (Fig. 15 or Suppl. Mat. A). The results suggest lateral composition symmetry, specifically the properties of deposited sizes, in relation to the central axis between the right (+) and left (−) sides of the basin. The strike lines show a clear, clean, unimodal and symmetric, Gaussian-like distribution of mean size, with a peak in the central axis. We observed a flattening of the curve at the central and distal strike lines, thus indicating a smaller standard deviation of the mean diameter deposited. In addition, we observed that the runs with high-flow rates (E30 and E40) presented larger diameters for the same location when compared with the lower flow rate run (E10), as also one might expect.

DISCUSSION

Recent studies have shown that the frequency of occurrence of turbidity currents is higher than previously proposed (Stevenson *et al.* 2018, Hage *et al.* 2019, Heijnen *et al.* 2022) and without the catastrophic characteristics reported for high turbulent turbidity currents (e.g., Mulder *et al.* 1997). Our observations led us to suggest the presence of at least two 3D characteristic lobe patterns for the distributary deposition of the experimental turbidity currents as a function of the input flow discharges tested. The first pattern is associated with the lower discharge tested (E10), whereas the second one is common to the other two remaining (higher) flow rates tried (E30-E40). While the case of E10 remains highly

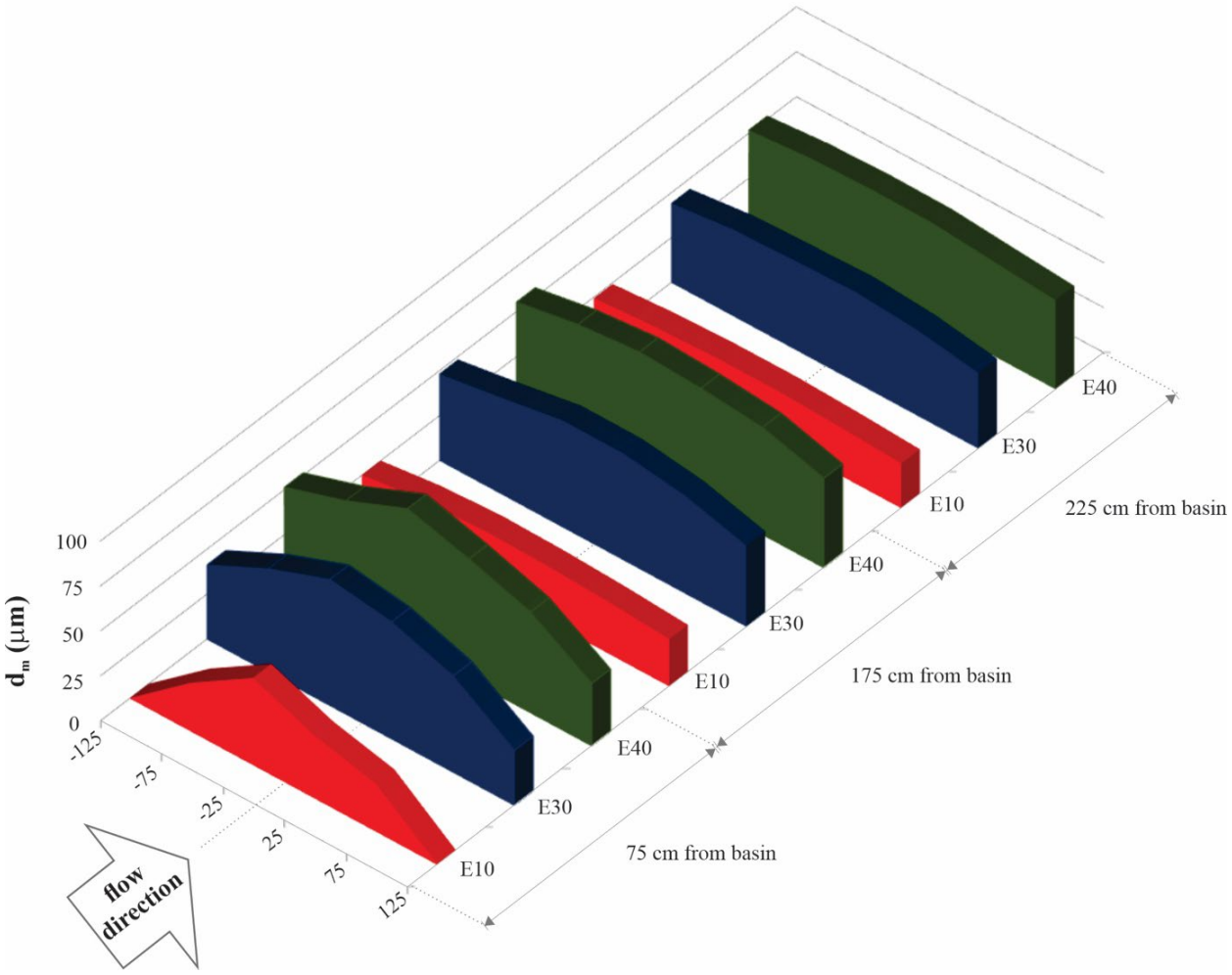

Figure 15. Mean diameter (d_m) of the deposit along the distance (strike section): at proximal (75 cm), central (175 cm), and distal (225 cm) positions, relative to unconfinement.

uncertain for upscaling due to the particularities of flow conditions in this run (e.g., laminar flow and possibly unrealistic for field scale, at least when considering channel-lobe transition, even for low-gradient cases). We nonetheless include the results with the note that further detailed research needs to be completed for a better understanding. We also advance some possible realistic field counterparts for this particular case, but with the important note that our remarks must remain marked as highly speculative. In addition, we note that an increment of 10 L/min between the experiments E30 and E40 was, presumably, not enough to significantly change overall properties, thus encouraging further studies.

To better describe the abovementioned (two) characteristic lobe patterns, the data collected for longitudinal velocity (X), transverse velocity (Y), and mean diameter (d_m) were used to create basin contour maps (Fig. 14) for visualization of the spatial variation of these different properties. Velocity maps started from the confinement exit (channel-lobe transition) in an attempt to minimize interpolation artifacts. The contour map of average velocities in the longitudinal direction (X) reveals two distinctly different behaviors as a function of the flow rate (Fig. 14A). For the lower flow rate (run E10), velocities were lower and decelerated throughout the basin, presenting maximum velocities along the central region of the formed lobe in a jet-like manner, as the same found in Manica *et al.* (2006) and Pohl *et al.* (2019). The flow spread out minimally, elongating downstream with little modification in the lateral lines. For higher flow rates (runs E30 and E40), velocities (both downstream and lateral) were higher (Fig. 14A), developing a higher variation in values over the lateral, and even more so at the end of the tank (3 m into the basin). At this position, a larger increase in velocity occurred on the sides compared to the central axis, possibly as a consequence of flow cascading (and accelerating) beyond the plate boundaries.

The average flow velocity contour map for the transverse direction (Y) is shown in Fig. 14B. As the current scattering angle can vary with flow characteristics (Baas *et al.* 2004), the resultant velocity and scattering angle can be represented by the velocity components on the X- and Y-axes. The spreading velocity of the current increased significantly with the increment of the flow rate, and for the highest flow rates (E30 and E40), there was symmetry of the values in relation to the center line of the basin. In the region immediately after the channel-lobe transition, the velocities in the transverse direction (Y) were about 300% higher than the velocities at the other points measured throughout the basin, which indicates that there was a remarkable overall deceleration of the turbidity current in a strike section, toward distal basin areas. Bell *et al.* (2021)

found the same trend, as the transversal velocities (strike) were abruptly decreasing (when compared with longitudinal velocities (dip). After initial spreading (up to 50 cm), where the central axis ADV captured some higher velocity values, the central velocity started to decrease as a result of the division of the flow into left and right directions (symmetrical). We note here that similar observations were also reported by Luthi (1981). In the low-flow rate run (E10), measurements and the map show anomalous, biased, relatively high velocities (Fig. 14B) on one side while no significant differences were observed in the resulting deposit, which leads us to maintain caution for further interpretation. Finally, the transverse velocity magnitude for E10 was 90% lower compared with the longitudinal magnitude.

The mean diameter (d_m) contour map (Fig. 14C) shows the most radial (short) zone of the lobe associated with the largest grain size class (silt and sand) for the higher flow rates (E30 and E40). At the lowest flow rate (E10), there is an elongation trending downward with the presence of silt. This indicates that the flow was not competent to carry coarser sediments downstream.

In fact, our results are consistent with some literature results. The mean diameters of the grains decreased as the distance in the longitudinal and transverse directions of the end of the confinement zone decreased, which had already been reported by Bouma (1962) and Luthi (1981). The tendency of the DSF to increase as the flow increases was in agreement with the results of Spychala *et al.* (2020). Even in the experiments carried out by this author, there was a slope break, with a confined slope zone immediately after injection of the mixture. Also, the Spychala *et al.*'s (2020) runs presented much higher concentrations and shorter duration compared to our runs.

Bell *et al.* (2021) reported that the coarser average diameters did not maintain a radial homogeneity on the lobe deposited, thus showing an elongated distribution of the grains. On contrary, the present results showed finite radial behavior (Fig. 14C). This difference is likely associated with the inclusion of microplastics and clay in the composition of the injected mixture, presence of slope break between regions, concentration difference, and the large difference between the flow rate values tested.

Overall, we note here that the higher discharge cases, defining one particular pattern, tended to create more "lobate" (rounded) deposits. A clear channel-lobe transition zone was identified where velocities were higher and the deposit showed a coarsening trend. The morphodynamics responses between deposit building (topography) and relatively higher flow inertial effects overcome this transition and interact with the topography. We did not observe the presence of internal hydraulic jumps or similar hydraulic transitions commonly described for higher gradient settings or slope breaks (e.g., Komar 1971). On contrary, we speculate that the lower discharge tested, the laminar flow case, could possibly have a field counterpart in principle in low-gradient, in very distal, terminal lobe settings associated with smaller distributary channels creating elongated, finger-like silty deposits, normally attributed in the literature to slurries (Hamilton *et al.* 2017, Lowe and Guy 2000, Bell *et al.* 2021). Based on this limited observation, one could explore the possibility of flows coming out of confinement from these smaller distributaries, and thus depositing elongated lobes, but where the realization of an almost laminar flow must be in principle sustained by a large increase in the flow concentration in a near-bed layer (*sensu* Felix and Peakall 2006, Manica 2012, Talling *et al.* 2012), thus increasing flow viscosity enough to suppress or limit turbulence to very low values, enough to maintain silt-size sediments in transport.

Flow deposit model

The contour maps (Fig. 14) showed the two-lobe patterns. In fact, there were no significant changes when comparing the E30 and E40 contour maps. Based on that, Fig. 16 summarizes these two cases. The low-flow rate (laminar) lobe pattern is associated with the following hydrodynamic characteristics: lower velocities in general, weak turbulence, subcritical behavior, elongated, low competence, and waning flow behavior along space (Kneller 1995). As turbidity currents flowed into the basin, they decelerated due to the deposition of the suspended load and became even less intense in terms of turbulence intensities (going more into the laminar flow regime). The associated deposit shows a clear elongated shape, with most possibly a lower flow regime plane bed and downstream fining. It is also safe to assume here that deposit building is controlled primarily by continuous deposition from the flow with less to no bedload transport volumes.

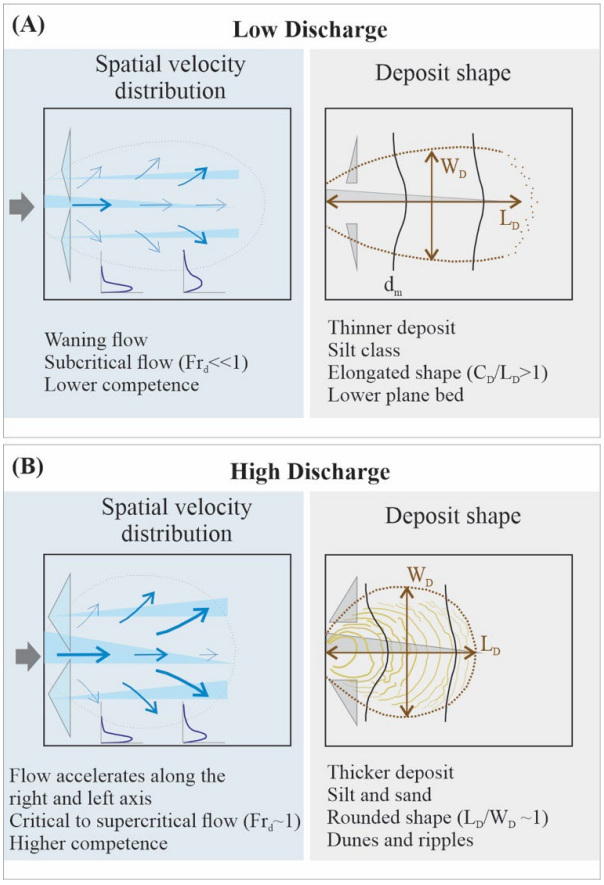

Figure 16. Low- and high-flow rate cause (flow) and effect (deposit) model proposed based on the experimental results.

Lobe generation by subcritical flows is less explored (e.g., Straub and Pyles 2012, Pickering and Hiscott 2016), although often observed in field situations. However, the low discharge case needs further in-depth investigation, particularly if related to laminar flow behavior, which might be in turn related to high concentration cases, very different than the conditions given in our experimental test E10.

On contrary, the high-flow lobe case presents a turbidity current with higher velocities, supercritical, turbulent, and higher competence. The flow tended to spread in all directions (radial), but it also presented typical characteristics of waning flows (Kneller 1995) with dilution and particle sedimentation. The formed deposit was more radial, marked by the presence of ripples and dunes, and downstream fining. Laterally, the same occurred up to the edge of the lobe.

In natural situations, this second type (or case) might describe a larger number of situations, including mid- to low-gradient settings and channels entering basins without significant slope breaks (Mulder *et al.* 1997, Mulder *et al.* 2003, Azpiroz-Zabala *et al.* 2017, Paull *et al*. 2018). In addition, it appears that supercritical (turbulent) flows might be more common in nature than thought before, even in low-gradient settings. We speculate since larger spreading rates, possibly flow thinning, and the absence of large energy dissipation at the channel-lobe transition due to a lack of internal hydraulic jump formation, these turbidity currents might remain critical-supercritical. The bedforms observed on the lobe tops of case 2 (dunes and ripples) are an indicator of supercritical flows (more energy), despite densimetric Froude numbers being close to one (critical). Subcritical, turbulent flow and associated deposits might remain more elusive, at least for the larger, lobe scale, in contrast to previous statements encountered in the literature (which remain largely untested).

CONCLUSION

Three-dimensional physical experiments carried out in this work allowed us to identify two characteristic lobe deposition models that were related to current flow rates, referred to as the low-flow case and the high-flow case, in a setting including channel-lobe transition without slope break. These experimentally derived models could in principle be, notwithstanding some clear limitations and constraints for applicability, extrapolated to the natural environment (as cause-consequence models). This study shows for the first time detailed hydraulic and sedimentologic measurements for describing the formation and evolution of lobe deposits in relatively low-gradient settings with the absence of slope breaks, which have been lacking up to date. The inferences and interpretations presented are only supported by a small set of trials, but nonetheless considered novel and revealing of fundamental behavior of the flows and associated sediment transport processes, under conditions that were mostly unexplored in a laboratory setting before. Finally, we emphasize the need for further detailed studies similar to the one presented here, in particular in relation to the cases involving subcritical, turbulent flows and associated turbidite deposits, which remain largely elusive from quantitative testing, and interpretations at the large scale (lobe) in the literature, highly speculative, at best.

ACKNOWLEDGMENTS

The first author thanks CNPQ for the financial support for his PhD study. Authors are thankful to Necod/IPH/UFRGS and ExxonMobil Upstream Research Group for all support on this research. Finally, the authors wish to express their gratitude to Léo A. Hartmann for his assistance and comments during the preparation of this manuscript.

ARTICLE INFORMATION

Manuscript ID: 20220029. Received on: 30 MAR 2022. Approved on: 6 OCT 2022.

How to cite this article: Guimarães T.M.H., Koller D.K., Fedele J.J., Manica R. 2022. Turbidity currents generating lobes: flow rate influence on 3D experiments without slope break. *Brazilian Journal of Geology*, **52**(4):e20220029. https://doi.org/10.1590/2317-4889202220220029

TMHG: essays, writing, interpretation of results. DKK: data interpretation, writing. JJF: writing, discussion. RM: data interpretation, writing.

Competing interest: the authors declare no competing interests.

REFERENCES

Altinakar M.S., Graf W.H., Hopfinger E.J. 1996. Flow structure in turbidity currents. *Journal of Hydraulic Research*, **34**(5):713-718. https://doi.org/10.1080/00221689609498467

Azpiroz-Zabala M., Cartigny M.J.B., Talling P.J., Parsons D.R., Sumner E.J., Clare M.A., Simmons S.M., Cooper C., Pope E.L. 2017. Newly recognized turbidity current structure can explain prolonged flushing of submarine canyons. *Science Advances*, **3**(10):1-12. https://doi.org/10.1126/sciadv.1700200

Baas J.H., Kesteren W.V., Postma G. 2004. Deposits of depletive high-density turbidity currents: a flume analogue of bed geometry, structure and texture. *Sedimentology*, **51**(5):1053-1088. https://doi.org/10.1111/j.1365-3091.2004.00660.x

Bell D., Soutter E.L., Cumberpatch Z.A., Ferguson R.A., Spychala Y.T., Kane I.A., Eggenhuisen J.T. 2021. Flow-process controls on grain type distribution in an experimental turbidity current deposit: Implications for detrital signal preservation and microplastic distribution in submarine fans. *The Depositional Record*, **7**(3):392-415. https://doi.org/10.1002/dep2.153

Bouma A.H. 1962. *Sedimentology of some flysch deposits: a graphic approach to facies interpretations*. Amsterdam, Elsevier, 168 p.

Castro C., Borges A.L.O., Manica R. 2021. A new empirical viscosity model for composed suspensions used in experiments of sediment gravity flows. *Brazilian Journal of Water Resources*, **26**, e22. https://doi.org/10.1590/2318-0331.262120210048

Clare M.A., Clarke J.E.H., Talling P.J., Cartigny M.J.B., Pratomo D.G. 2016. Preconditioning and triggering of offshore slope failures and turbidity currents revealed by most detailed monitoring yet at a fjord-head delta. *Earth and Planetary Science Letters*, **450**:208-220. https://doi.org/10.1016/j.epsl.2016.06.021

Cooper C., Wood J., Andrieux A. 2013. Turbidity current measurements in the Congo Canyon, OTC Abstract 23992. *In*: Offshore Technology Conference, 2013, Houston, Texas. *Procedures*, 12 p.

Fabian S. 2002. *Modelagem física de correntes de densidade conservativas em canal de declividade variável*. MS Dissertation, Postgraduate Program in Water Resources and Environmental Sanitation, Universidade Federal do Rio Grande do Sul, Porto Alegre, 119 p.

Fedele J.J., Hoyal D.C., Barnaal Z., Tulenko J., Awalt S. 2016. Bedforms created by gravity flows. *In*: Budd D.A., Hajek E.A., Purkis S.J. (eds.), *Autogenic dynamics and self-organization in sedimentary systems*. SEPM Special Publication, v. 106, p. 95-121. https://doi.org/10.2110/sepmsp.106.12

Felix M., Peakall J. 2006. Transformation of debris flow into turbidity currents: mechanisms interfered from laboratory experiments. *Sedimentology*, **53**(1):107-123. https://doi.org/10.1111/j.1365-3091.2005.00757.x

Ferreira P.L.C. 2013. *Análise comparativa entre correntes de densidade e jatos*. MS Dissertation, Postgraduate Program in Water Resources and Environmental Sanitation, Universidade Federal do Rio Grande do Sul, Porto Alegre.

Hage S., Cartigny M.J.B., Sumner E.J., Clare M.A., Clarke J.E.H., Talling P.J., Lintern D.G., Simmons S.M., Jacinto R.S., Vellinga A.J., Allin J.R., Azpiroz-Sabala M., Gales J.A., Hizzett J.L., Hunt J.E., Mozzato A., Parsons D.R., Pope E.L., Stacey C.D., Symons W.O., Vardy M.E., Watts C. 2019. Direct monitoring reveals initiation of turbidity currents from extremely dilute river plumes. *Geophysical Research Letters*, **46**(20):11310-11320. https://doi.org/10.1029/2019GL084526

Hamilton P., Gaillot G., Strom K., Fedele J., Hoyal D. 2017. Linking hydraulic properties in supercritical submarine distributary channels to depositional lobe geometry. *Journal of Sedimentary Research*, **87**(9):935-950. https://doi.org/10.2110/jsr.2017.53

Heijnen M.S., Clare M.A, Cartigny M.J.B., Talling P.J., Hage S., Pope E.L., Bailey L., Sumner E., Lintern D.G., Stacey C., Parsons D.R., Simmons S.M., Chen Y., Hubbard S.M., Eggenhuisen J.T., Kane I., Clarke J.E.H. 2022. Fill, flush or shuffle: How is sediment carried through submarine channels to build lobes? *Earth and Planetary Science Letters*, **584**:117481. https://doi.org/10.1016/j.epsl.2022.117481

Hodgson D.M. 2009. Distribution and origin of hybrid beds in sand-rich submarine fans of the Tanqua depocentre, Karoo Basin, South Africa. *Marine and Petroleum Geology*, **26**(10):1940-1956. https://doi.org/10.1016/j.marpetgeo.2009.02.011

Jobe Z.R., Sylvester Z., Parker A.O., Howes N., Pirmez C. 2015. Rapid adjustment of submarine channel architecture to changes in sediment supply. *Journal of Sedimentary Research*, **85**(6):729-753. https://doi.org/10.2110/jsr.2015.30

Kneller B. 1995. Beyond the turbidite paradigm: physical models for deposition of turbidites and their implications for reservoir prediction *In*: Hartley A.J., Prosser D.J. (eds.), *Characterization of Deep-Marine Clastic Systems*. London: Geological Society, Special Publications, v. 94(1), p. 31-49. https://doi.org/10.1144/GSL.SP.1995.094.01.04

Kneller B., Buckee C. 2000. The structure and fluid mechanics of turbidity currents: a review of some recent studies and their geological implications. *Sedimentology*, **47**(Suppl. 1):62-94. https://doi.org/10.1046/j.1365-3091.2000.047s1062.x

Koller D.K., Manica R., Borges A.O.L., Fedele J.J. 2019. Experimental bedforms by saline density currents. *Brazilian Journal of Geology*, **49**(2):e20180118. https://doi.org/10.1590/2317-4889201920180118

Komar P.D. 1971. Hydraulic jumps in turbidity currents. *Geological Society of America Bulletin*, **82**(6):1477-1488. https://doi.org/10.1130/0016-7606(1971)82[1477:HJITC]2.0.CO;2

Leeuw J., Eggenhuisen J.T., Cartigny M.J.B. 2016. Morphodynamics of submarine channel inception revealed by new experimental approach. *Nature Communications*, **7**:10886. https://doi.org/10.1038/ncomms10886

Lowe D.R., Guy M. 2000. Slurry-flow deposits in the Britannia Formation (lower Cretaceous), North Sea: a new perspective on the turbidity current and debris flow problem. *Sedimentology*, **47**(1):31-70. https://doi.org/10.1046/j.1365-3091.2000.00276.x

Luthi S. 1981. Experiments on non-channelized turbidity currents and their deposits. *Marine Geology*, **40**(3-4):M59-M68. https://doi.org/10.1016/0025-3227(81)90139-0

Manica R. 2012. Sediment gravity flows: study based on experimental simulations *In*: Schulz H.E., Simões A.L.A., Lobosco R.J. (Eds.), *Hydrodynamics: Natural Water Bodies*. London: IntechOpen, p. 263-286. https://doi.org/10.5772/28794

Manica R., Maestri R.D., Borges A.L.O. 2006. Modelagem física de correntes de turbidez: descrição do processo e implicações no estudo dos depósitos turbidíticos. *Pesquisas em Geociências*, **33**(2):19-33. https://doi.org/10.22456/1807-9806.19510

Middleton G.V. 1966. Small-scale models of turbidity currents and the criterion for auto-suspension. *Journal of Sedimentary Petrology*, **36**(1):202-208.

Mulder T., Alexander J. 2001. The physical character of subaqueous sedimentary density flows and their deposits. *Sedimentology*, **48**(2):269-299. https://doi.org/10.1046/j.1365-3091.2001.00360.x

Mulder T., Etienne S. 2010. Lobes in deep-sea turbidite systems: State of the art. *Sedimentary Geology*, **229**(3):75-80. https://doi.org/10.1016/j.sedgeo.2010.06.011

Mulder T., Savoye B., Syvitski J.P.M. 1997. Numerical modelling of a mid-sized gravity flow: the 1979 Nice turbidity current (dynamics, processes, sediment budget and seafloor impact). *Sedimentology*, **44**(2):305-326. https://doi.org/10.1111/j.1365-3091.1997.tb01526.x

Mulder T., Syvitski J.P.M., Migeon S., Faugères J.C., Savoye B. 2003. Marine hyperpycnal flows: initiation, behavior and related deposits. A review. *Marine Petroleum Geology*, **20**(6-8):861-882. https://doi.org/10.1016/j.marpetgeo.2003.01.003

Normark W.R. 1970. Growth patterns of deep-sea fans. *American Association of Petroleum Geologists Bulletin*, **54**(11):2170-2195. https://doi.org/10.1306/5D25CC79-16C1-11D7-8645000102C1865D

Paull C.K., Talling P.J., Maier K.L., Parsons D., Xu J., Caress D.W., Gwiazda R., Lundsten E.M., Anderson K., Barry J.P., Chaffey M., O'Reilly T., Rosenberger K.J., Gales J.A., Kieft B., McGann M., Simmons S.M., McCann M., Sumner E.J., Clare M.A., Cartigny J.M. 2018. Powerful turbidity currents driven by dense basal layers. *Nature Communications*, **9**(1):4114. https://doi.org/10.1038/s41467-018-06254-6

Pettingill H.S. 2004. Global overview of deep-water exploration and production. *In*: Weimer P., Pettingill H.S., Nilsen T.H. (eds.). *Petroleum Systems of Deepwater Settings*. Society of Exploration Geophysicists and European Association of Geoscientists and Engineers, p. 1-40. https://doi.org/10.1306/St571314C2

Pickering K., Hiscott R. 2016. Deep marine systems: processes, deposits, environments, tectonics and sedimentation. Wiley & American Geophysical Union.

Piper D.J.W., Normark W.R. 2009. Processes that initiate turbidity currents and their influence on turbidites: a marine geology perspective. *Journal of Sedimentary Research*, **79**(6):347-362. https://doi.org/10.2110/jsr.2009.046

Piper D.J.W., Savoye B. 1993. Processes of late Quaternary turbidity current flow and deposition on the Var deep-sea fan, north-west Mediterranean Sea. *Sedimentology*, **40**(3):557-582. https://doi.org/10.1111/j.1365-3091.1993.tb01350.x

Pohl F., Eggenhuisen J.T., Tilston M., Cartigny M.J.B. 2019. New flow relaxation mechanism explains scour fields at the end of submarine channels. *Nature Communications*, **10**:4425. https://doi.org/10.1038/s41467-019-12389-x

Postma G., Hoyal D.C., Abreu V., Cartigny M.J.B., Demko T., Fedele J.J., Kleverlaan K., Pederson K.H. 2016. Morphodynamics of supercritical turbidity currents in the channel-lobe transition zone. *In*: Lamarche G., Mountjoy J., Bull S., Hubble T., Krastel S., Lane E., Micallef A., Moscardelli L., Mueller C., Pecher I., Woelz S. (eds.), *Submarine Mass Movements and their Consequences*. Advances in Natural and Technological Hazards Research. Switzerland: Springer International, v. 41, p. 469-478. https://doi.org/10.1007/978-3-319-20979-1_47

Shepard F.P. 1981. Submarine canyons: multiple causes and long-time persistence. *AAPG Bulletin*, **65**(6):1062-1077. https://doi.org/10.1306/03B59459-16D1-11D7-8645000102C1865D

Simpson J.E. 1972. Effects of the lower boundary on the head of a gravity current. *Journal of Fluid Mechanics*, **53**(4):759-768. https://doi.org/10.1017/S0022112072000461

Spychala Y.T., Eggenhuisen J.T., Tilston M., Pohl F. 2020. The influence of basin setting and turbidity current properties. *Sedimentology*, **67**(7):3471-3491. https://doi.org/10.1111/sed.12751

Stevenson C.J., Feldens P., Georgiopoulou A., Schönke M., Krastel S., Piper D.W.D., Lindhorst K., Mosher D. 2018. Reconstructing the sediment concentration of a giant submarine gravity flow. *Nature Communications*, **9**:2616. https://doi.org/10.1038/s41467-018-05042-6

Straub K.M., Pyles D.R. 2012. Quantifying the hierarchical organization of compensation in submarine fans using surface statistics. *Journal of Sedimentary Research*, **82**(11):889-898. https://doi.org/10.2110/jsr.2012.73

Sweet M.L., Gaillot G.T., Jouet G., Rittenour T.M., Toucanne S., Marsset T., Blum M.D. 2019. Sediment routing from shelf to basin floor in the Quaternary Golo System of Eastern Corsica, France, western Mediterranean Sea. *Geological Society of America Bulletin*, **132**(5-6):1217-1234. https://doi.org/10.1130/B35181.1

Talling P.J., Bake M.L., Pope E.L, Ruffell S.C., Jacinto R.S., Heijnen M.S., Hage S., Simmons S.M., Hasenhundl M., Heerema C.J., McGhee C., Apriloual R., Ferrant A., Cartigny M.J.B., Parsons D.R., Clare M.A., Tshimanga R.M., Trigg M.A., Cula C.A., Faria R., Gaillot A., Wallance D., Griffiths A., Nunny R., Urlanb M., Burnett R., Neasham J., Hilton R.J. 2022. Longest sediment flows yet measured show how major rivers connect efficiently to deep sea. *Nature Communications*, **13**:4193. https://doi.org/10.1038/s41467-022-31689-3

Talling P.J., Masson D.G., Sumner E.J., Malgesini G. 2012. Subaqueous sediment density flows: depositional processes and deposit types. *Sedimentology*, **59**(7):1937-2003. https://doi.org/10.1111/j.1365-3091.2012.01353.x

Talling P.J., Paull C.K., Piper D.J.W. 2013. How are subaqueous sediment density flows triggered, what is their internal structure and how does it evolve? Direct observations from monitoring of active flows. *Earth-Science Reviews*, **125**:244-287. https://doi.org/10.1016/j.earscirev.2013.07.005

Xu J.P., Sequeiros O.E., Noble M.A. 2014. Sediment concentrations, flow conditions, and downstream evolution of two turbidity currents, Monterey Canyon, USA. *Deep-Sea Research Part I: Oceanographic Research Papers*, **89**:11-34. https://doi.org/10.1016/j.dsr.2014.04.001